

Analysis of noise-induced errors in vector-field electron tomographyZ. D. C. Kemp,^{1,*} T. C. Petersen,^{1,2} D. M. Paganin,¹ K. M. Spiers,³ M. Weyland,^{2,4} and M. J. Morgan¹¹*School of Physics, Monash University, Victoria 3800, Australia*²*Monash Centre for Electron Microscopy, Monash University, Victoria 3800, Australia*³*Australian Synchrotron, Clayton, Victoria 3168, Australia*⁴*Department of Materials Engineering, Monash University, Victoria 3800, Australia*

(Received 12 May 2014; published 29 August 2014)

Vector-field electron tomography (VFET) reconstructs electromagnetic vector fields of magnetic nanomaterials using transmission electron microscopy. The theory behind this reconstruction process is well established, but the practical implications of experimental errors and how they affect the accuracy of the reconstructed vector fields is not well understood, hindering progress in the use of these techniques for routine magnetic characterization of nanomaterials. Here, we present an analysis of the propagation of stochastic errors through a VFET algorithm. A method for determining the contribution of image noise to errors in a reconstructed vector potential is derived. Simulations are performed to test the validity of this method when applied to shot noise, which shows good agreement with theory.

DOI: [10.1103/PhysRevA.90.023859](https://doi.org/10.1103/PhysRevA.90.023859)

PACS number(s): 42.30.Rx, 81.70.Tx, 41.20.Gz

I. INTRODUCTION

Vector-field electron tomography (VFET) is a relatively new technique for three-dimensional (3D) magnetic imaging, combining phase retrieval with vector tomography to reconstruct electromagnetic vector fields from transmission electron micrographs [1–3]. The characterization of magnetic nanomaterials is a crucial aspect of a wide range of topical areas of research, including spintronics [4], biomedical nanotechnology [5], magnetic recording media [6], and the development of nanomotors [7].

There are many experimental techniques for the characterization of magnetic nanomaterials, such as Kerr microscopy [8], magnetic exchange force microscopy [9], and spin-polarized scanning tunneling microscopy [10], which can be employed to examine components of the magnetization on the surface of the sample. Lorentz transmission electron microscopy (LTEM) has significant advantages over these techniques in that it can be used to probe the *internal* magnetic structure of a sample [11]. Using LTEM, the phase of the electron wave function at the exit surface of the magnetic specimen can be measured from out-of-focus micrographs or electron holograms, but this provides only two-dimensional projections of the potentials. VFET combines LTEM with tomography (the reconstruction of an object function from its projections) to enable a complete, 3D magnetic characterization of the sample. For example, VFET can be used to reconstruct all three components of the vector potential of a magnetic nanoparticle at all points inside, and around, a sample [12].

Conventional scalar tomography has been employed for decades as a means to probe the internal structure of 3D objects. X-ray computed tomography and positron emission tomography are routinely used as medical diagnostic tools, but scalar tomography has also proved extremely useful in a diverse range of other fields. Examples include the imaging of microscopic biological samples using synchrotron radiation [13] and transmission electron microscopy [14], structural characterization of semiconductor devices using scanning

transmission electron microscopy [15], 3D imaging of binary stars using Doppler measurements [16], delineation of magma bodies using seismic tomography [17], and 3D imaging of macroscopic mechanical parts using neutron tomography [18].

The theory of scalar tomography has been extended to the reconstruction of vector fields [19]. The majority of the work on vector tomography relates to the use of acoustic time-of-flight or Doppler measurements to reconstruct fluid flows. Such applications include the imaging of blood flow [20], flue gas velocity in coal-fired power stations [21], and water velocity in lakes [22]. VFET is the application of vector tomography to electromagnetic vector fields, such as magnetic fields, magnetic vector potentials, and current densities [12], using the transmission electron microscope (TEM). VFET requires information of the phase shift induced in the electron beam as it traverses an electromagnetic sample. The exit phase of the beam is measured over two or more tilt series and is used to tomographically reconstruct the vector fields in three dimensions. This requires the phase to be reconstructed from intensity measurements, which can be performed using off-axis electron holography [23] or propagation-based phase retrieval [24].

The theoretical foundations of VFET are well established, with the process having been employed to experimentally reconstruct magnetic nanomaterials [2,25]. However, there are numerous artifacts in these reconstructions, and while there are many known sources of error, including image noise, image misalignment, and technical limitations that result in a missing wedge of information in each tilt series, the propagation of these errors through the reconstruction process is not well understood.

In this work, we consider one significant source of error, namely, shot noise in the recorded micrographs. The effect of image noise on the reconstructed vector field has been briefly investigated by Yu *et al.* [3]. Their work tested the stability of various VFET algorithms when white Poisson noise was added to simulated micrographs, noting qualitative features of the noise-induced artifacts in the reconstructed vector fields.

A significant source of error in VFET reconstructions is the amplification of noise near Fourier-space singularities in both the phase retrieval and vector tomography algorithms. The

*zachary.kemp@monash.edu

effects of noise can be ameliorated by regularization of these singularities. The results obtained by Yu *et al.* [3] provide a means to identify certain noise-induced artifacts, which they found can occur in the form of streaking in the reconstructed vector potential, which result from the presence of the singularities in the reconstruction algorithms. However, their work did not provide a quantitative analysis of the propagation of noise-induced errors through the reconstruction. Indeed, a quantitative analysis of the propagation of noise through these algorithms has not been presented in the literature. In this work, we address the limitations of previous work by providing a thorough, quantitative, and analytical study of the propagation of image noise through a VFET algorithm.

Here, we derive expressions to calculate expected VFET reconstruction errors as a function of image noise. We use three different root-mean-square (rms) error metrics to quantify the total reconstruction error, and the errors in the direction and magnitude of the reconstructed vectors, separately. We compare the errors predicted using these analytical models with those measured from VFET reconstructions performed using simulated micrographs.

Owing to the large amount of data required and technical considerations, such as alignment of the tilt series, VFET can be a time-consuming and computationally demanding process; consequently, it is important to have a thorough understanding of how variables such as spatial resolution and image acquisition time affect accuracy. This is a key motivation for this work.

We close this introduction with a brief overview of the remainder of the paper. Section II presents the theoretical foundations of VFET, from phase retrieval to tomographic reconstruction, including relevant considerations such as the nature of shot noise. In Sec. III, we define the rms error metrics used to quantify the accuracy of our reconstructions, and derive analytical expressions for these errors as a function of image noise. In Sec. IV, we present errors calculated from tomographically reconstructed vector fields using simulated micrographs, and compare these with our analytical results. We make some concluding remarks in Sec. V.

II. THEORETICAL BACKGROUND

In the TEM, electromagnetic information about the sample is encoded in the phase of the electron wave function at the exit surface via the Aharonov-Bohm effect. The contribution

to the phase shift due to the electrostatic potential $V(\mathbf{r}_\perp, z)$ is given by [26]

$$\varphi_e(\mathbf{r}_\perp) = \frac{\pi}{E\lambda} \int V(\mathbf{r}_\perp, z) dz, \quad (1)$$

where z is the distance along the optical axis, \mathbf{r}_\perp is a position vector in the plane normal to the optical axis, E is the electron accelerating potential, and λ is the electron wavelength. The contribution to the phase shift due to the magnetic vector potential $\mathbf{A}(\mathbf{r}_\perp, z)$ is given by [27]

$$\varphi_m(\mathbf{r}_\perp) = -\frac{e}{\hbar} \int \mathbf{A}(\mathbf{r}_\perp, z) \cdot d\mathbf{z}, \quad (2)$$

where e is the magnitude of the electron's charge, and \hbar is the reduced Planck constant. Under the projection approximation, these two components of the phase shift can be interpreted as projections of the electrostatic potential and the magnetic vector potential, respectively. Here, we consider projections to be straight line integrals of the vector potential in the electron propagation direction. This definition is consistent with the projection approximation of electron holography, which ensures applicability of the projection-slice theorem (which underpins the reconstruction algorithm). Measuring φ_m from micrographs at multiple angles over two tilt series provides a way to reconstruct the vector potential. A schematic of the experimental setup is shown in Fig. 1. In the remainder of this section we discuss the theory of the processes used to perform the reconstruction, from phase retrieval to vector tomography, as well as regularization and shot noise.

A. Phase retrieval using the transport of intensity equation (TIE)

In order to obtain projections of the vector potential for its reconstruction, the phase must be inferred from recorded micrographs. This can be achieved using off-axis holography [23] or propagation-based phase retrieval [24]. We use the latter for our simulations. Specifically, a transport of intensity equation (TIE) algorithm is used to compute the phase from simulated out-of-focus micrographs. In addition to being computationally efficient, this method is linear under the phase object approximation. This simplifies the analysis of the propagation of errors from the micrographs to the phase, relative to iterative methods such as the Gerchberg-Saxton algorithm [28]. The TIE relates transverse phase gradients to

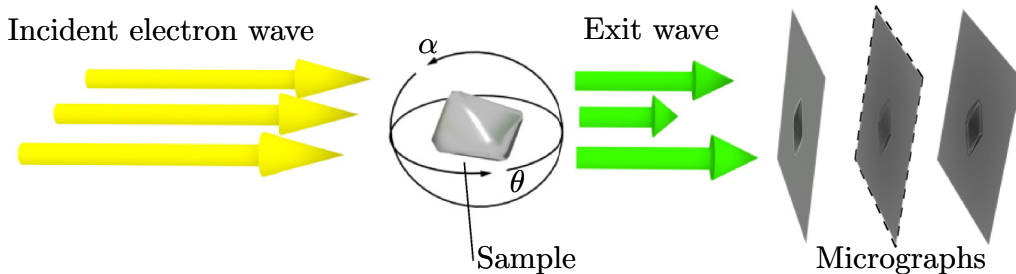


FIG. 1. (Color online) Schematic of the experimental setup. The exit phase of the electron wave is modified by the potentials of the sample, and is measured by recording out-of-focus micrographs and applying a phase retrieval algorithm. The focal plane image (indicated by a dashed border) is approximated from the underfocus (left) and overfocus (right) micrographs. The exit phase is measured for multiple angles about two orthogonal axes (α and θ), enabling reconstruction of the vector potential associated with the sample.

the longitudinal derivative of the intensity [27]:

$$-k \frac{\partial I_0}{\partial z} = \nabla_{\perp} \cdot (I_0 \nabla_{\perp} \varphi_0), \quad (3)$$

where k is the wave number, I_0 and φ_0 are the intensity and phase at the image plane ($z = 0$), respectively, and

$$\frac{\partial I_0}{\partial z} \equiv \left. \frac{\partial I(\mathbf{r}_{\perp}, z)}{\partial z} \right|_{z=0}. \quad (4)$$

To obtain the phase, given measurements of both I_0 and $\frac{\partial I_0}{\partial z}$, Eq. (3) can be solved using a Fourier-transform method [24]

$$\varphi(\mathbf{r}_{\perp}) = \frac{k}{4\pi^2} \mathcal{F}^{-1} \left\{ \frac{\mathbf{k}}{|\mathbf{k}|^2} \cdot \mathcal{F} \left[\frac{1}{I_0} \mathcal{F}^{-1} \left(\mathbf{k} \frac{\mathcal{F}(\frac{\partial I_0}{\partial z})}{|\mathbf{k}|^2} \right) \right] \right\}, \quad (5)$$

where \mathbf{k} is the spatial frequency, and \mathcal{F} and \mathcal{F}^{-1} denote the two-dimensional Fourier transform and its inverse, respectively. Under the phase object approximation, when the object is very weakly attenuating, the in-focus intensity I_0 can be replaced with the incident intensity I^{in} , hence [29]

$$\varphi(\mathbf{r}_{\perp}) = \frac{k}{4\pi^2 I^{\text{in}}} \mathcal{F}^{-1} \left\{ \frac{\mathcal{F} \left\{ \frac{\partial I_0}{\partial z} \right\}}{|\mathbf{k}|^2} \right\}. \quad (6)$$

This approximation is sufficient for the purposes of noise analysis [30]. For the simulations performed here, both Eqs. (5) and (6) are used separately to compare the results of each with analytical results derived using Eq. (6). For the former, the approximation

$$I_0 \approx \frac{I(\mathbf{r}_{\perp}, \Delta f) + I(\mathbf{r}_{\perp}, -\Delta f)}{2\Delta f} \quad (7)$$

is used, which reduces the number of images required from three to two. The longitudinal derivative of the intensity can be approximated from out-of-focus micrographs. For this work, due to its simplicity and computational efficiency, a two-image central difference method is employed, i.e.,

$$\frac{\partial I_0}{\partial z} = \frac{I(\mathbf{r}_{\perp}, \Delta f) - I(\mathbf{r}_{\perp}, -\Delta f)}{2\Delta f}. \quad (8)$$

The phase obtained using the TIE contains information about both the magnetic and electrostatic properties of the sample. For the purposes of reconstructing the vector potential, it is only the magnetic component that is of interest. There are multiple methods to obtain this. The dependence of the electrostatic phase shift on the electron wavelength can be exploited to obtain the magnetic phase by varying the accelerating potential [31]. Another method assumes that the electrostatic phase shift is proportional to the sample thickness, and uses the in-focus image to calculate the electrostatic contribution and remove it from the total retrieved phase [32]. The separation of the magnetic and electrostatic phases can also be achieved by flipping the sample and recording additional micrographs with the electron beam now traveling in the opposite direction relative to the sample. This allows the magnetic component of the phase to be extracted by exploiting the different time-reversal symmetries of the electrostatic and magnetic Aharonov-Bohm shifts [33]. For phase retrieval using the TIE, this separation can be applied to the micrographs themselves [34], or to the retrieved phases [35]. We use the

latter method, for which

$$\varphi_{\text{mag}} = \frac{\varphi_f - \varphi_r}{2}, \quad (9)$$

where φ_f and φ_r are the phase shifts imparted by the sample before and after flipping, respectively. Experimentally, φ_r is obtained by rotating the sample by 180° about an axis orthogonal to z , and reversing the resulting phase maps about the axis of rotation.

B. Vector tomography

Tomography is the reconstruction of an object function from its projections. Scalar tomography typically takes a series of projections about a single tilt axis and reconstructs a scalar function from these projections. Vector tomography requires the acquisition of additional tilt series to obtain enough information about the specimen to reconstruct a vector field in three dimensions.

For this work, the vector potential $\mathbf{A}(x, y, z)$ is reconstructed using a filtered back projection (FBP) algorithm, which uses the projection-slice theorem in cylindrical coordinates, in combination with the Coulomb gauge condition. This algorithm is given by [3]

$$\begin{aligned} \mathbf{A}(x, y, z) = & \int_0^\pi \int_{-\infty}^\infty \int_{-\infty}^\infty \frac{\tilde{T}^\theta |k_r^\theta| k_r^\theta}{k_x^2 + k_y^2 + k_z^2} \begin{bmatrix} \frac{k_y^2 + k_z^2}{k_y} \\ -k_x \\ \frac{k_x k_z}{k_y} \end{bmatrix} \\ & \times e^{2\pi i [k_r^\theta (x \cos \theta + y \sin \theta) + k_z z]} dk_r^\theta dk_z d\theta \\ & + \int_0^\pi \int_{-\infty}^\infty \int_{-\infty}^\infty \frac{\tilde{T}^\alpha |k_r^\alpha| k_r^\alpha}{k_x^2 + k_y^2 + k_z^2} \begin{bmatrix} \frac{k_x k_z}{k_y} \\ k_z \\ \frac{-k_x^2 - k_y^2}{k_y} \end{bmatrix} \\ & \times e^{2\pi i [k_r^\alpha (y \cos \alpha + z \sin \alpha) + k_x x]} dk_r^\alpha dk_x d\alpha, \end{aligned} \quad (10)$$

where θ and α are positive angles of rotation about the z and x axes, respectively, T^θ and T^α are the tilt series associated with these directions, tildes represent Fourier-transformed quantities, and $k_r^\theta = k_y / \sin \theta$ and $k_r^\alpha = k_y / \cos \alpha$ are radial spatial frequencies. T^θ and T^α are given by [3]

$$T^\theta(x, z) = -\frac{\hbar}{e} \varphi_m(x, z) \quad (11)$$

and

$$T^\alpha(y, x) = -\frac{\hbar}{e} \varphi_m(y, x). \quad (12)$$

The geometry for tilt series acquisition is shown in Fig. 2.

In practice, a discrete form of Eq. (10) is used for the reconstruction. For this work, we perform the reconstructions on a cubic voxel grid, and it is convenient to make a change of variables which enables the algorithm to be expressed as three summations. Given this, the algorithm we use can be expressed as

$$\begin{aligned} \mathbf{A}_{m,n,p} = & \frac{\pi}{n_t - 1} \sum_{\mu=0}^{n_t-1} \frac{1}{M^2} \sum_{l,j=-M/2}^{M/2-1} \\ & \times (\tilde{T}^\theta \eta_{l,j,\mu}^\theta e^{2\pi i (ln' + jp)/M} + \tilde{T}^\alpha \eta_{l,j,\mu}^\alpha e^{2\pi i (ln'' + jm)/M}), \end{aligned} \quad (13)$$

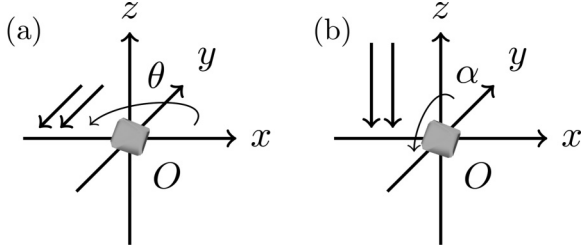


FIG. 2. Acquisition of tilt series T^θ and T^α . The curved arrows indicate the direction that the object O is rotated in each tilt series, and the double arrows indicate the propagation direction of the electron beam (after Yu *et al.* [3]).

where M is the number of pixels along each direction of the input images; n_t is the number of magnetic phase maps in each tilt series; m , n , and p are the voxel indices in real space; $n' = m \cos \theta + n \sin \theta$; and $n'' = n \cos \alpha + p \sin \alpha$. The coefficients $\eta_{l,j,\mu}^\theta$ and $\eta_{l,j,\mu}^\alpha$ are given by

$$\eta_{l,j,\mu}^\theta = \frac{l^2}{aM(l^2 + j^2)} \begin{bmatrix} \frac{l^2 \sin^2 \theta + j^2}{l \sin \theta} \\ -l \cos \theta \\ -j \cot \theta \end{bmatrix} \quad (14)$$

and

$$\eta_{l,j,\mu}^\alpha = \frac{l^2}{aM(l^2 + j^2)} \begin{bmatrix} j \tan \alpha \\ l \sin \alpha \\ -\frac{l^2 \cos^2 \alpha + j^2}{l \cos \alpha} \end{bmatrix}. \quad (15)$$

Here, a is the width of the input micrographs, and θ and α are both given by $\pi\mu/(n_t - 1)$. Bilinear interpolation is used to transform from radial to Cartesian coordinates. The inverse discrete Fourier transforms implicit in Eq. (13) can be computed using a fast-Fourier-transform algorithm (see, for example, Ref. [36]).

C. Regularization of singularities

The phase retrieval and FBP algorithms used here contain Fourier-space singularities, resulting in numerical instability and amplification of noise. In order to overcome these problems, solutions can be forced to be finite at the singularities by modifying the algorithms using regularization. In previous work [37], Tikhonov regularization [38] has been employed to deal with the singularity in Eq. (5) at $|\mathbf{k}| = 0$, and we follow this approach. This is achieved by applying the following transformation to Eq. (6):

$$|\mathbf{k}|^2 \rightarrow \frac{|\mathbf{k}|^4 + \delta_{\text{TIE}}^4}{|\mathbf{k}|^2}, \quad (16)$$

where δ_{TIE} is a regularization parameter having dimensions of a reciprocal length. We obtain

$$\varphi(\mathbf{r}_\perp, 0) = \frac{k}{4\pi^2 I^{\text{in}}} \mathcal{F}^{-1} \left\{ \frac{|\mathbf{k}|^2 \mathcal{F} \left\{ \frac{\partial I_0}{\partial z} \right\}}{|\mathbf{k}|^4 + \delta_{\text{TIE}}^4} \right\}. \quad (17)$$

This makes the solution finite at $|\mathbf{k}| = 0$, allowing numerical computation, and also suppresses amplification of noise near $|\mathbf{k}| = 0$. For $|\mathbf{k}|/\delta_{\text{TIE}} \gg 1$, Eq. (17) reduces to Eq. (6), but at (and near) $|\mathbf{k}| = 0$, the regularized TIE deviates from the exact

solution. Because the regularization does not arise naturally from the theory, it induces errors in the reconstruction. Finding an appropriate choice for a regularization parameter is a compromise between choosing a large enough value to adequately suppress errors, while keeping it small enough to remain consistent with the theory and avoiding unnecessarily introducing artifacts from the regularization itself. Tikhonov regularization is employed wherever singularities occur in the algorithms. For Eq. (5), the transformation used is

$$|\mathbf{k}|^2 \rightarrow \frac{|\mathbf{k}|^4 + \delta_{\text{TIE}}^4/2}{|\mathbf{k}|^2}. \quad (18)$$

We have introduced the factor of 2 for consistency in the scale of the regularization parameters. That is, we require that the results obtained using Eq. (5) match those of Eq. (6) when $I_0 = I^{\text{in}}$. The use of Eq. (18) for the former and Eq. (16) for the latter ensures this, provided that δ_{TIE} is small.

Equation (10) contains singular surfaces at $k_y = 0$ for A_x and A_z . In terms of the tilt angles, these singular surfaces are at $\theta = 0$ and $\alpha = \pi/2$. Due to the practical limitations of recording tilt series over the entire range of π radians, it is natural to remove the singular surface at $\theta = 0$ by simply omitting this image from the reconstruction process. For the singular surface at $\alpha = \pi/2$, we again use Tikhonov regularization:

$$\frac{1}{\cos \alpha} \rightarrow \frac{\cos \alpha}{\cos^2 \alpha + \delta_{\text{FBP}}^2}, \quad (19)$$

where δ_{FBP} is the regularization parameter.

The division by I_0 in Eq. (5) can also cause numerical instability in the presence of noise. We address this by regularizing with

$$I_0 \rightarrow \frac{I_0^2 + \delta_{\text{INT}}^2}{I_0}, \quad (20)$$

where δ_{INT} is the regularization parameter. Because noise in I_0 does not impact greatly on the errors in the reconstruction, the choice of δ_{INT} does not affect the noise-induced errors examined in this work. We arbitrarily set $\delta_{\text{INT}} = 0.08 I^{\text{in}}$, which is small enough to avoid introducing significant systematic errors in the retrieved phases.

The recorded micrographs are subject to shot noise due to the finite number of electrons recorded at the detector. Shot noise is dependent on beam current and acquisition time [39], and propagates through the phase retrieval process. Singularities in the phase retrieval algorithm can amplify the noise, and the methods of regularization, as well as the parameters used, can be chosen for optimal suppression of this amplification.

D. Shot-noise model

Previous work on the effects of noise in VFET used a white Gaussian [1] or Poisson [3] noise model. These models treat the noise level as a constant, with no variation across the image. In our work, we use a more realistic shot-noise model that takes into account the change in noise level with changing intensity and provides a more accurate distribution of noise over the simulated images, particularly for large defocus and/or when there is significant attenuation.

The scale used for the intensity is arbitrary, and is proportional to the mean number of detected electrons per pixel. Thus, we can define a constant of proportionality κ such that

$$I^{\text{in}} = \kappa N, \quad (21)$$

where N is the mean number of detected electrons per pixel in the absence of a sample. The noise-free intensity $I_{l,j}^{\text{ideal}}$ at a given pixel is related to the mean number of detected electrons $N_{l,j}$ at that pixel by

$$I_{l,j}^{\text{ideal}} = \kappa N_{l,j}. \quad (22)$$

The actual intensity, taking shot noise into account, is then

$$I_{l,j} = \kappa \Pi(N_{l,j}), \quad (23)$$

where $\Pi(N_{l,j})$ produces a random integer selected from a Poisson distribution with mean $N_{l,j}$. This leads to the relation

$$\frac{I_{l,j}}{I_{l,j}^{\text{ideal}}} = \frac{\Pi(N_{l,j})}{N_{l,j}}. \quad (24)$$

From Eqs. (21) and (22), the mean number of detected electrons is

$$N_{l,j} = \frac{I_{l,j}^{\text{ideal}}}{I^{\text{in}}} N. \quad (25)$$

Substituting this into Eq. (24), the intensity is then given by

$$I_{l,j} = \Pi\left(\frac{I_{l,j}^{\text{ideal}}}{I^{\text{in}}} N\right) \frac{I^{\text{in}}}{N}. \quad (26)$$

We define an incident noise level

$$\sigma_{\text{in}} = \frac{\sqrt{N}}{N}, \quad (27)$$

which is the fractional noise level in a micrograph recorded in the absence of a sample. This results in slightly underestimated noise levels when the sample is highly attenuating, but more closely matches an experimental scenario where the beam current, acquisition time, and detector behavior is typically the same for every image. The intensity in the noisy image is then

$$I_{l,j} = \Pi\left(\frac{I_{l,j}^{\text{ideal}}}{\sigma_{\text{in}}^2 I^{\text{in}}}\right) \sigma_{\text{in}}^2 I^{\text{in}}. \quad (28)$$

III. PROPAGATION OF SHOT NOISE THROUGH A VECTOR-FIELD ELECTRON TOMOGRAPHY ALGORITHM

Quantifying errors in reconstructed vector fields differs from quantifying those of scalar reconstructions in that the total error involves errors due to differences in the magnitude of the input and output vector at each voxel, and differences in the orientation of the vectors. What makes a reconstruction accurate depends on the application. For example, for some applications, the magnitude of the vector potential may be of little interest, and accuracy is only required for the direction of the reconstructed vectors. For other applications, it may be important to know the accuracy of the magnitude of the vectors. Other quantities that may be of interest include the curl and divergence of the vector field, and metrics can also

be chosen to highlight the accuracy of a reconstructed field in terms of these quantities.

For this work, we use three different metrics to quantify the errors. The first is designed to quantify the total difference between the exact and reconstructed vector fields, and the other two are motivated by two attributes that may be of particular interest, namely, direction and magnitude, respectively. The total normalized rms error metric is defined by

$$E^{\text{tot}} = \sqrt{\frac{\sum_{i,j,k} |\mathbf{A}_{i,j,k}^{\text{rec}} - \mathbf{A}_{i,j,k}|^2}{\sum_{i,j,k} |\mathbf{A}_{i,j,k}|^2}}, \quad (29)$$

where \mathbf{A}^{rec} is the reconstructed vector potential. Our directional rms error is defined as the rms value of the angle between the exact and reconstructed vectors at each voxel and is given by

$$E^{\text{dir}} = \sqrt{\frac{1}{M^3 \pi^2} \sum_{i,j,k} \left[\cos^{-1} \left(\frac{\mathbf{A}_{i,j,k} \cdot \mathbf{A}_{i,j,k}^{\text{rec}}}{|\mathbf{A}_{i,j,k}| |\mathbf{A}_{i,j,k}^{\text{rec}}|} \right) \right]^2}, \quad (30)$$

where the factor of π is included so that E^{dir} is expressed as a fractional error rather than an angle. The normalized rms error in the magnitude of the vector potential is given by

$$E^{\text{mag}} = \sqrt{\frac{\sum_{i,j,k} (|\mathbf{A}_{i,j,k}^{\text{rec}}| - |\mathbf{A}_{i,j,k}|)^2}{\sum_{i,j,k} |\mathbf{A}_{i,j,k}|^2}}. \quad (31)$$

In simulations, the noise-induced component $E_{\text{noise}}^{\text{tot}}$ of the normalized total rms error can be extracted using

$$E_{\text{noise}}^{\text{tot}} = \sqrt{E^{\text{tot}}(\sigma_{\text{in}})^2 - E^{\text{tot}}(0)^2}. \quad (32)$$

The noise-induced components of the directional and magnitude errors, $E_{\text{noise}}^{\text{dir}}$ and $E_{\text{noise}}^{\text{mag}}$, respectively, can be obtained in the same manner. In the remainder of this section, we derive analytical expressions for $E_{\text{noise}}^{\text{tot}}$, $E_{\text{noise}}^{\text{dir}}$, and $E_{\text{noise}}^{\text{mag}}$.

A. Effect of shot noise on total RMS errors

Ignoring other sources of error, we can express the reconstructed vector field at a given voxel as

$$\mathbf{A}_{i,j,k}^{\text{rec}} = \mathbf{A}_{i,j,k} + \mathbf{A}_{i,j,k}^{\text{noise}}, \quad (33)$$

where $\mathbf{A}^{\text{noise}}$ is the noise-induced component of the vector field.

Substituting Eq. (33) into Eq. (29), $E_{\text{noise}}^{\text{tot}}$ can be obtained by calculating

$$E_{\text{noise}}^{\text{tot}} = \sqrt{\frac{\sum_{i,j,k} |\mathbf{A}_{i,j,k}^{\text{noise}}|^2}{\sum_{i,j,k} |\mathbf{A}_{i,j,k}|^2}} = \sqrt{\frac{M^3 \sigma_{\text{out}}^2}{\sum_{i,j,k} |\mathbf{A}_{i,j,k}|^2}}, \quad (34)$$

where σ_{out} is the standard deviation of the noise-induced reconstruction error. Equation (34) is valid for large M . In deriving an analytical model for σ_{out} , we utilize the noise variance analysis of McDowell *et al.* [40]. In the case of phase retrieval using the TIE, the input signal is the longitudinal derivative $\partial_z I$ of the intensity across the image plane. The error in $\partial_z I$ due to noise, when two defocused micrographs are

used to approximate the derivative, is given by [30]

$$\sigma'_{\text{in}} = \frac{\sigma_{\text{in}}}{\sqrt{2}\Delta f}. \quad (35)$$

To determine σ_{out} , we express the noise in the Fourier transform of the through focal derivatives as a random complex number $c_{l,j}$ with variance

$$\langle c_{l,j} c_{l,j}^* \rangle = I_0^2 \sigma_{\text{in}}^2, \quad (36)$$

where $\langle \dots \rangle$ denotes the expectation value. It is worth noting that, by virtue of being the Fourier transform of a real function (the noise in the through focal derivatives), $c_{l,j}$ has the Hermitian property

$$c_{l,j} = c_{-l,-j}^*, \quad (37)$$

but this does not affect our derivation. In practice, a white noise model will not be sufficient to accurately predict errors from all sources of noise that may be present. For this reason, we introduce the filter functions H^θ and H^α to account for the spectrum of the image noise in each tilt series; if this is independent of defocus, these filters applied to the approximated through focal derivatives are identical to

those applied to the images used to calculate them. These functions can also incorporate any additional filtering that is performed in an effort to reduce the effects of noise on the reconstruction. Considering only errors due to noise, the Fourier-transformed through focal derivatives constructed from experimental micrographs are then given by

$$\partial_z \tilde{I}_{l,j,\mu}^\theta = \partial_z \tilde{I}_{l,j,\mu}^{\text{ideal},\theta} + \frac{\hbar}{e} H_{l,j,\mu}^\theta c_{l,j,\mu}^\theta \quad (38)$$

and

$$\partial_z \tilde{I}_{l,j,\mu}^\alpha = \partial_z \tilde{I}_{l,j,\mu}^{\text{ideal},\alpha} + \frac{\hbar}{e} H_{l,j,\mu}^\alpha c_{l,j,\mu}^\alpha, \quad (39)$$

where $\partial_z \tilde{I}^{\text{ideal},\theta}$ and $\partial_z \tilde{I}^{\text{ideal},\alpha}$ are the noise-free components of $\partial_z \tilde{I}^\theta$ and $\partial_z \tilde{I}^\alpha$, respectively.

Noting the linearity of the reconstruction algorithm [Eq. (13)], and considering Eqs. (33), (38), and (39), we can immediately write an expression for the noise-induced component of the reconstructed vector field:

$$\mathbf{A}_{m,n,p}^{\text{noise}} = \frac{\pi}{n_t - 1} \sum_{\mu=0}^{n_t-1} \frac{1}{M^2} \sum_{l,j=-M/2}^{M/2-1} \frac{\hbar}{e} (H_{l,j,\mu}^\theta \eta_{l,j,\mu}^\theta c_{l,j} e^{2\pi i(\ln'+jp)/M} + H_{l,j,\mu}^\alpha \eta_{l,j,\mu}^\alpha c_{l,j} e^{2\pi i(\ln''+jm)/M}). \quad (40)$$

The variance σ_{out}^2 in each voxel of the reconstruction is the second moment of $\mathbf{A}^{\text{noise}}$:

$$\sigma_{\text{out}}^2 = \frac{\hbar^2}{e^2 q} \left\langle \left[\frac{\pi}{(n_t - 1)} \sum_{\mu=0}^{n_t-1} \left(\frac{1}{M^2} \sum_{l,j=-M/2}^{M/2-1} \zeta_{l,j} (H_{l,j,\mu}^\theta \eta_{l,j,\mu}^\theta e^{2\pi i(\ln'+jp)/M} + H_{l,j,\mu}^\alpha \eta_{l,j,\mu}^\alpha e^{2\pi i(\ln''+jm)/M}) c_{l,j} \right) \right]^2 \right\rangle, \quad (41)$$

where q is the number of phase maps used to obtain a single magnetic phase map (typically $q = 2$) and

$$\zeta_{l,j} = \frac{a^2 M^2 k}{I_0 4\pi^2 (l^2 + j^2)} \quad (42)$$

is the spatial frequency response of the phase retrieval algorithm under the phase object approximation. The noise is uncorrelated between phase maps both within, and between, tilt series, which leads to the result

$$\sigma_{\text{out}}^2 = \frac{I_0^2 \sigma_{\text{in}}^2 \pi^2 \hbar^2}{q M^4 (n_t - 1)^2 e^2} \times \sum_{\mu=0}^{n_t-1} \sum_{l,j=-M/2}^{M/2-1} H_{l,j}^2 \zeta_{l,j}^2 (|\eta_{l,j,\mu}^\theta|^2 + |\eta_{l,j,\mu}^\alpha|^2), \quad (43)$$

where we have made use of Eq. (36). In practice, the spatial frequency spectrum of the noise may be a function of tilt series and angle, but for simplicity, we assume that it is a function only of spatial frequencies, and have removed these dependencies in H . We treat the Poisson noise in our simulations as being approximately uniform, and set $H = 1$ in our analytical calculations.

The summations in Eq. (43) can be computed very quickly, and require no knowledge of the properties of the sample. Any

regularization scheme can also be easily incorporated, which enables the effects of regularization on errors due to noise to be calculated quickly.

B. Effect of shot noise on directional rms errors

In this section, we derive approximations for the contribution to E^{dir} due to noise. Substituting Eq. (33) into (30), the directional error is given by

$$E_{\text{noise}}^{\text{dir}} = \sqrt{\frac{1}{M^3 \pi^2} \sum_{i,j,k} \left[\cos^{-1} \left(\frac{|\mathbf{A}_{i,j,k}| + \hat{\mathbf{A}}_{i,j,k} \cdot \mathbf{A}_{i,j,k}^{\text{noise}}}{|\mathbf{A}_{i,j,k} + \mathbf{A}_{i,j,k}^{\text{noise}}|} \right) \right]^2}, \quad (44)$$

where the circumflex is used to denote a unit vector. The magnitude of the reconstructed vector can be determined using the cosine rule, and is given by

$$|\mathbf{A}_{i,j,k} + \mathbf{A}_{i,j,k}^{\text{noise}}| = |\mathbf{A}_{i,j,k}| \sqrt{1 + \frac{|\mathbf{A}_{i,j,k}^{\text{noise}}|^2}{|\mathbf{A}_{i,j,k}|^2} + 2 \frac{\hat{\mathbf{A}}_{i,j,k} \cdot \mathbf{A}_{i,j,k}^{\text{noise}}}{|\mathbf{A}_{i,j,k}|}}. \quad (45)$$

Substituting this into Eq. (44), and using the binomial approximation, gives

$$E_{\text{noise}}^{\text{dir}} = \sqrt{\frac{1}{M^3 \pi^2} \sum_{i,j,k} \left\{ \cos^{-1} \left[\left(1 + \frac{\hat{\mathbf{A}}_{i,j,k} \cdot \mathbf{A}_{i,j,k}^{\text{noise}}}{|\mathbf{A}_{i,j,k}|} \right) \left(1 - \frac{|\mathbf{A}_{i,j,k}^{\text{noise}}|^2}{2|\mathbf{A}_{i,j,k}|^2} - \frac{\hat{\mathbf{A}}_{i,j,k} \cdot \mathbf{A}_{i,j,k}^{\text{noise}}}{|\mathbf{A}_{i,j,k}|} \right) \right] \right\}^2}. \quad (46)$$

We now introduce the notation

$$R_{i,j,k} \equiv \frac{\mathbf{A}_{i,j,k} \cdot \mathbf{A}_{i,j,k}^{\text{noise}}}{|\mathbf{A}_{i,j,k}| |\mathbf{A}_{i,j,k}^{\text{noise}}|}. \quad (47)$$

Here, $R_{i,j,k}$ is a random variable on the interval $[-1, 1]$ which, if the orientation of $\mathbf{A}_{i,j,k}^{\text{noise}}$ is *uniformly* random, has a probability density given by

$$\begin{aligned} p(R_{i,j,k}) &= \frac{1}{\pi} \left| \frac{d}{dx} \cos^{-1} x \right|_{x=R_{i,j,k}} \\ &= \begin{cases} \frac{1}{\pi \sqrt{1-R_{i,j,k}^2}}, & -1 < R_{i,j,k} < 1 \\ 0, & \text{elsewhere.} \end{cases} \end{aligned} \quad (48)$$

Discarding terms of $\mathcal{O}(|\mathbf{A}_{i,j,k}^{\text{noise}}|^3)$ in Eq. (46) gives

$$E_{\text{noise}}^{\text{dir}} = \sqrt{\frac{1}{M^3 \pi^2} \sum_{i,j,k} \left\{ \cos^{-1} \left[1 - \left(R_{i,j,k}^2 + \frac{1}{2} \right) \frac{|\mathbf{A}_{i,j,k}^{\text{noise}}|^2}{|\mathbf{A}_{i,j,k}|^2} \right] \right\}^2}, \quad (49)$$

and the approximation

$$\cos^{-1}(1-x) \approx \sqrt{2x}, \quad (50)$$

valid for small x (i.e., low-noise levels), simplifies this to

$$E_{\text{noise}}^{\text{dir}} = \sqrt{\frac{1}{M^3 \pi^2} \sum_{i,j,k} |\mathbf{A}_{i,j,k}^{\text{noise}}|^2 \left(\frac{\sqrt{2R_{i,j,k}^2 + 1}}{|\mathbf{A}_{i,j,k}|} \right)^2}. \quad (51)$$

Using the binomial approximation, and discarding terms of $\mathcal{O}(|\mathbf{A}_{i,j,k}^{\text{noise}}|^2)$, gives

$$\begin{aligned} E_{\text{noise}}^{\text{mag}} &= \sqrt{\frac{\sum_{i,j,k} R_{i,j,k}^2 |\mathbf{A}_{i,j,k}^{\text{noise}}|^2}{\sum_{i,j,k} |\mathbf{A}_{i,j,k}|^2}} \\ &= \sigma_{\text{out}} \sqrt{\frac{\sum_{i,j,k} R_{i,j,k}^2}{\sum_{i,j,k} |\mathbf{A}_{i,j,k}|^2}} = \frac{E_{\text{noise}}^{\text{tot}}}{\sqrt{2}}. \end{aligned} \quad (56)$$

The rms value of $|\mathbf{A}_{i,j,k}^{\text{noise}}|$ is σ_{out} , while that of $\sqrt{2R_{i,j,k}^2 + 1}$ is $\sqrt{2}$, and because these are assumed to be independent, they can be evaluated separately to give

$$E_{\text{noise}}^{\text{dir}} = \sqrt{\frac{2}{M^3 \pi^2} \sum_{i,j,k} \frac{\sigma_{\text{out}}^2}{|\mathbf{A}_{i,j,k}|^2}} \approx \frac{\sqrt{2}}{\pi} E_{\text{noise}}^{\text{tot}}, \quad (52)$$

where we have made use of the approximation

$$\frac{1}{M^3} \sum_{i,j,k} \frac{\sigma_{\text{out}}^n}{|\mathbf{A}_{i,j,k}|^n} \approx (E_{\text{noise}}^{\text{tot}})^n, \quad (53)$$

which is valid when $|\mathbf{A}_{i,j,k}|$ is approximately constant for all i, j, k . This requirement implies that Eq. (52) may be inaccurate for geometries where the magnitude of the vector potential varies significantly over the domain of reconstruction. For example, a pair of uniformly magnetized particles with antiparallel moments has large $|\mathbf{A}_{i,j,k}|$ near each particle, but decays quickly outside the specimen, and directional errors calculated in this way may be significantly less accurate than for a single dipole.

Because we have dropped higher-order terms in the derivation of $E_{\text{noise}}^{\text{dir}}$, the accuracy of Eq. (52) in approximating noise-induced errors is expected to be poor for large $\sigma_{\text{in}}/\Delta f$. For accurate results in this region, the $\mathcal{O}(|\mathbf{A}_{i,j,k}^{\text{noise}}|^3)$ terms in Eq. (46) can be retained, to give the improved approximation

$$E_{\text{noise}}^{\text{dir}} = \frac{E_{\text{noise}}^{\text{tot}}}{\pi} \sqrt{2 + E_{\text{noise}}^{\text{tot}}/2}, \quad (54)$$

where we have again made use of Eq. (53).

C. Effect of shot noise on rms errors in magnitude

Substituting Eq. (45) into (31), we get

$$E_{\text{noise}}^{\text{mag}} = \sqrt{\frac{\sum_{i,j,k} |\mathbf{A}_{i,j,k}|^2 \left[(1 + |\mathbf{A}_{i,j,k}^{\text{noise}}|^2/|\mathbf{A}_{i,j,k}|^2 + 2R_{i,j,k} |\mathbf{A}_{i,j,k}^{\text{noise}}|/|\mathbf{A}_{i,j,k}|)^{1/2} - 1 \right]^2}{\sum_{i,j,k} |\mathbf{A}_{i,j,k}|^2}}. \quad (55)$$

IV. COMPARISON OF RECONSTRUCTION ERRORS: SIMULATIONS AND ANALYTICAL RESULTS

In this section, we present analytical estimates for reconstruction errors, based on the analysis presented in Sec. III, and compare these with the errors in reconstructions performed on simulated TEM data. There are a multitude of parameters that affect reconstruction errors, and these are too numerous to address comprehensively here. For this reason, we restrict our attention to the variation of two parameters of significance, namely, defocus and image noise.

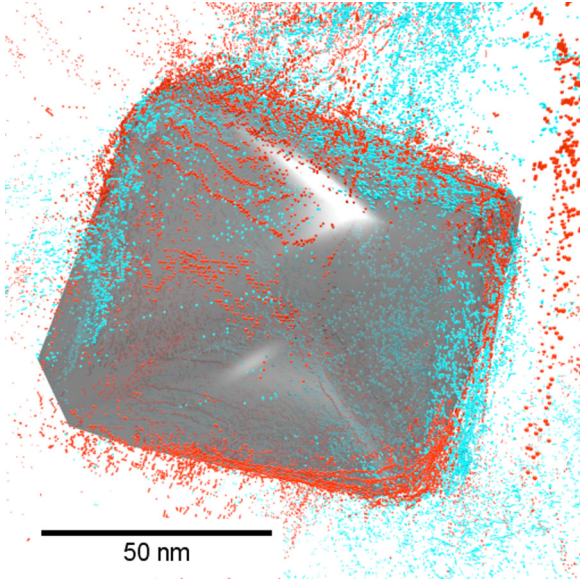


FIG. 3. (Color online) Shape of sample mask used for our simulations (gray) and surface point cloud obtained using scalar tomography [42] applied separately to two tilt series [red (dark gray) and blue (light gray)]. For an animated version of this figure, see Supplemental Material [43].

For our simulations, the sample shape was measured from experimental scalar tomograms of an octahedral magnetite nanoparticle. The nanoparticles were produced by dissolving $\text{FeSO}_4 \cdot 7\text{H}_2\text{O}$ in water and initiating precipitation using potassium hydroxide and potassium nitrate, according to the procedure described in Ref. [41]. The resulting dry magnetite powder was mixed with ethanol, placed in an ultrasonic bath, and then dispersed onto a holey carbon TEM support using a pipette. Specimen charging was observed, so the nanoparticles were covered with approximately 5 nm of carbon in a Gatan 682 precision etching and coating system, which noticeably reduced spurious charging effects.

The specimen was loaded into an FEI Titan 80–300 kV TEM, operated at 300 kV in the bright field Lorentz imaging

modality. Using 5° angular increments over $\pm 65^\circ$, a tilt series of bright field images was acquired at a nominal defocus of $-10 \mu\text{m}$, using a dedicated Fischione 2040 dual-axis tomography holder. With the same angular sampling and range, another tilt series was collected after first rotating the specimen by 90° in plane at a nominal defocus of $+10 \mu\text{m}$. All images were aligned using cross-correlation algorithms. Defocus-induced rotations between the overfocused and underfocused images were corrected by optimizing the height of cross-correlation peaks, in response to induced relative rotations between image pairs using bilinear interpolation. For each of the two mutually orthogonal tilt series, defocus derivatives were computed and used as input for surface tomography reconstruction of the nanoparticle morphology. The implicit Laplacian-based contrast in the defocus derivatives served as ideal input for image-processing ridge detection since the straight edges of the nanoparticle polyhedron were clearly highlighted in the experimental data. The unstructured point cloud data from both tomograms was combined to partly fill the missing wedge. For details of the reconstruction algorithm used, see Ref. [42].

The simulated sample was constructed by tracing the surface of the particle in three dimensions using 3D modeling software (Blender 2.67). The shape of the simulated sample, along with the experimental tomograms from which it was constructed, is shown in Fig. 3.

A mean inner potential of 17 V [44], mass magnetization of 80 emu/g [45], and density of 5.18 g/cm^3 [46] were chosen to simulate a magnetite sample. An imaginary potential of 0.8i V, inferred from the experimental micrographs of the sample being simulated, was added to the mean inner potential to simulate attenuation. These parameters were used to calculate total phase shifts using the projection approximation, and defocused images were then obtained by means of a transfer function [47]. Shot noise of the form given by Eq. (28) was then added to the simulated micrographs.

Figure 4 shows a through focal derivative computed from simulated micrographs, along with one computed from experimental micrographs of the actual sample.

Underfocus and overfocus micrographs were simulated for every θ and α , with $M = 64$ and $n_t = 31$. After the addition

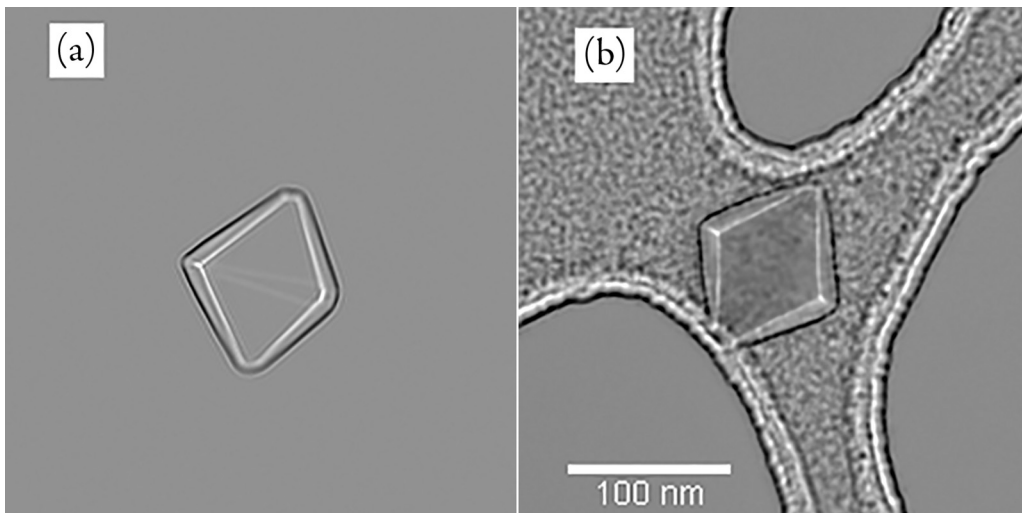


FIG. 4. Example of through focal derivatives computed from micrographs with $\Delta f = -10 \mu\text{m}$ and $\sigma_{\text{in}} = 1\%$ using (a) simulated micrographs and (b) experimental micrographs.

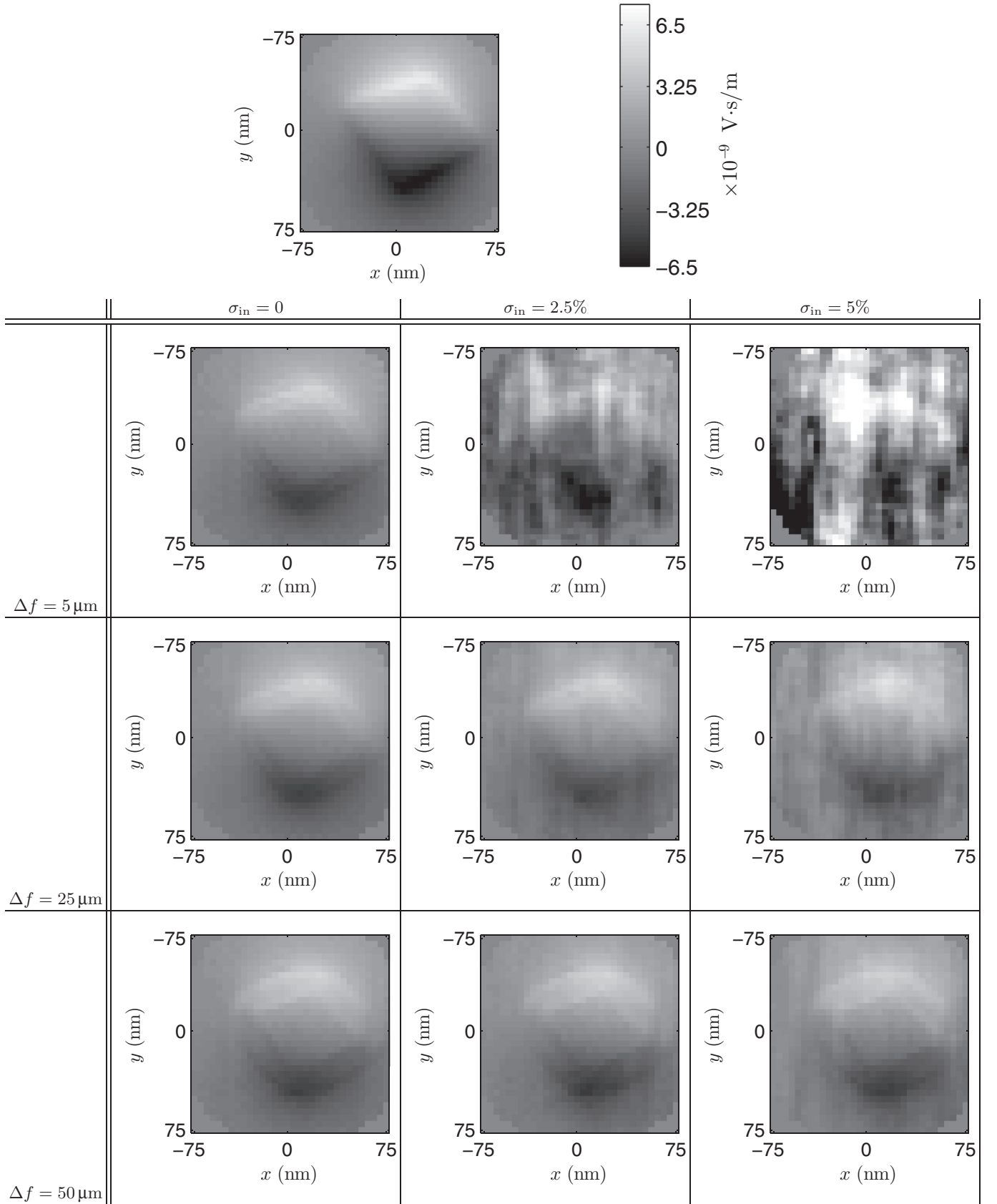


FIG. 5. Slice of the x component of the exact vector potential at $z = 0$ (top), and the same slice taken from reconstructions using various values of Δf and σ_{in} .

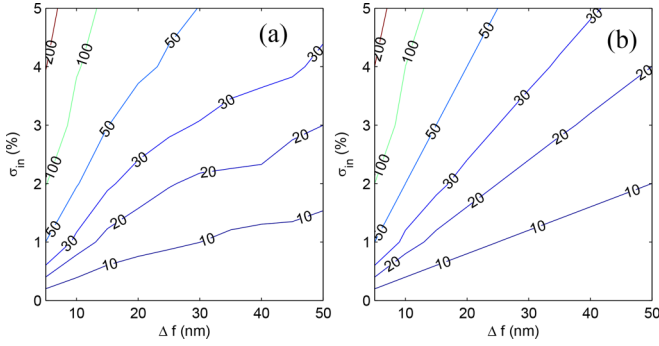


FIG. 6. (Color online) Contour plots of $E_{\text{noise}}^{\text{tot}}$ as a function of σ_{in} and Δf for (a) reconstructions using simulated data, obtaining the phase via Eq. (5), and (b) analytical results obtained using Eqs. (34) and (43). The numbers given on the contour lines are total rms errors expressed as a percentage.

of noise, the micrographs were used to retrieve the phases that comprise T^θ and T^α . $\mathbf{A}(\mathbf{r})$ was reconstructed using Eq. (13), and then used to calculate $E_{\text{noise}}^{\text{tot}}$, $E_{\text{noise}}^{\text{dir}}$, and $E_{\text{noise}}^{\text{mag}}$. These simulations were performed for a range of σ_{in} and Δf . Each simulation was performed 10 times for each σ_{in} and Δf , with the results averaged, to suppress fluctuations about the mean rms error for large σ_{in} . The x component of the exact vector potential is shown alongside that of the reconstructed vector potentials, for various combinations of Δf and σ_{in} , in Fig. 5.

The predictive power of our analysis is quantified using a normalized residual metric defined by

$$\chi^{\text{tot}} = (\bar{E}_{\text{noise}}^{\text{tot}} - E_{\text{noise}}^{\text{tot}}) / E_{\text{noise}}^{\text{tot}}, \quad (57)$$

where the macron denotes the analytically derived estimate. For the accuracy of $E_{\text{noise}}^{\text{dir}}$ and $E_{\text{noise}}^{\text{mag}}$, the metrics χ^{dir} and χ^{mag} are similarly defined.

Figure 6 shows $E_{\text{noise}}^{\text{tot}}$ and $\bar{E}_{\text{noise}}^{\text{tot}}$, respectively, as contour plots over σ_{in} and Δf . It is evident that increasing the image noise will result in increased reconstruction errors, as the errors due to noise in the micrographs propagate through the reconstruction algorithm and translate to noisy reconstruction data. The reduction in error as the defocus is increased is less intuitive. This occurs because phase contrast in the micrographs increases with increasing defocus, provided that the defocus is not too large in magnitude. When σ_{in} remains constant, the ratio of the noise level to the phase contrast signal drops as the defocus is increased, and this results in a reduced noise-induced error in the phase [30]. It is this error that then propagates to the reconstructed vector field.

The contour plots in Fig. 6 are presented to provide an overview of how the total reconstruction error depends on image noise and defocus, in both the simulated and analytical results. For the results that follow, we use 3D surface plots to represent the error data because they provide a clearer comparison between simulated and analytical results, and serve to better highlight the regions in which these results deviate from each other.

Figure 7 shows surface plots comparing the analytically derived estimates $\bar{E}_{\text{noise}}^{\text{tot}}$, obtained using Eq. (43) in conjunction with Eq. (34), with $E_{\text{noise}}^{\text{tot}}$ obtained from the reconstruction of simulated micrographs by applying Eqs. (29) and (32). These

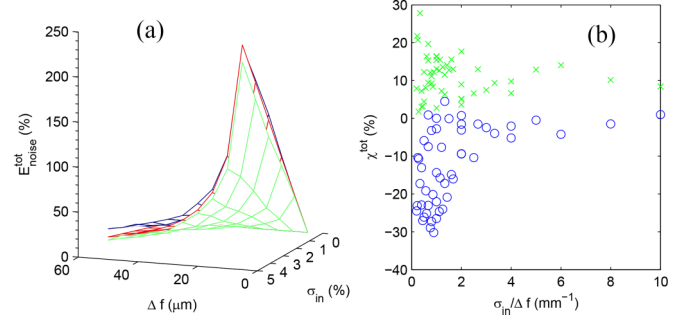


FIG. 7. (Color online) (a) Analytically derived values $\bar{E}_{\text{noise}}^{\text{tot}}$ [red (dark gray)] obtained using Eqs. (34) and (43), along with the results of simulations $E_{\text{noise}}^{\text{tot}}$ using Eq. (5) for the phase retrieval [blue (black)] and Eq. (6) [green (light gray)]. (b) Normalized residual χ^{tot} plotted against $\sigma_{\text{in}}/\Delta f$ for each method (blue circles and green crosses, respectively).

represent the same data presented in Fig. 6, with the addition of simulated results where the reconstruction relied on the phase object approximation.

Because $I_{i,j}^{\text{ideal}}$ varies across the image, the noise level is not, in practice, constant. However, for the analytical calculations here, $H_{i,j}$ is set to unity for simplicity, approximating the noise as uniformly distributed.

The strong agreement between analytical results and simulations shows that Eq. (43) can be used to accurately predict rms errors from the signal-to-noise ratio of transmission electron micrographs, and can be used to determine

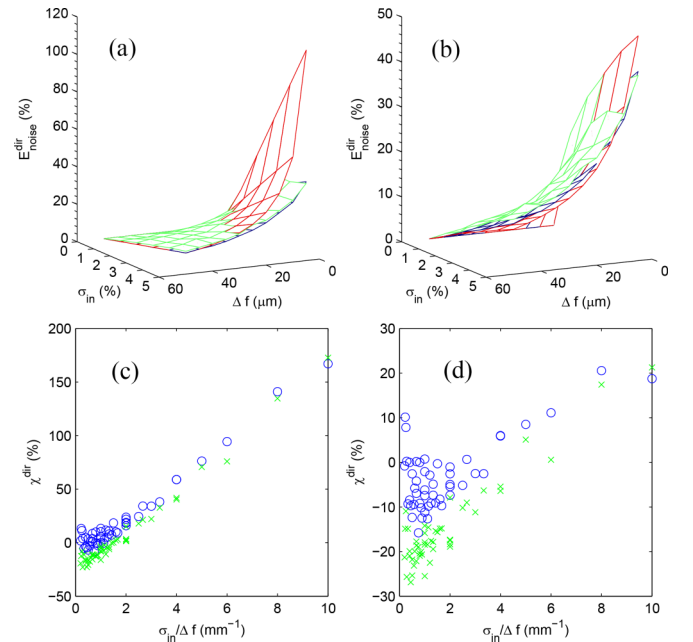


FIG. 8. (Color online) Analytically derived values $\bar{E}_{\text{noise}}^{\text{dir}}$ [red (dark gray)], along with the results of simulations $E_{\text{noise}}^{\text{dir}}$ using Eq. (5) for the phase retrieval [blue (black)], and Eq. (6) [green (light gray)]; (a) using the approximation given by Eq. (52), and (b) using the higher-order approximation given by Eq. (54). (c), (d) Normalized residual χ^{dir} plotted against $\sigma_{\text{in}}/\Delta f$ for each approximation, respectively, showing both the results obtained using Eqs. (5) (blue circles) and (6) (green crosses).

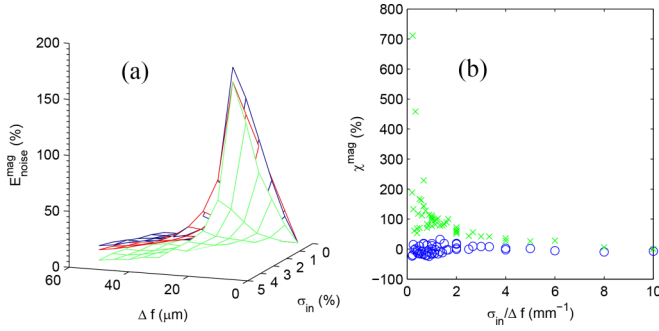


FIG. 9. (Color online) (a) Analytically derived values $\bar{E}_{\text{noise}}^{\text{abs}}$ obtained using Eq. (56) [red (dark gray)], along with the results of simulations $E_{\text{noise}}^{\text{abs}}$ using Eq. (5) for the phase retrieval [blue (black)], and Eq. (6) [green (light gray)]. (b) Normalized residual χ^{abs} plotted against $\sigma_{\text{in}}/\Delta f$ for each method (blue circles and green crosses, respectively).

minimum experimental acquisition times required to keep the reconstruction errors due to noise below a desired limit. It can also be used to quickly compute the noise-induced errors for a variety of experimental parameters. These results also show that, under the conditions used in these simulations, shot noise is adequately modeled as white noise.

Figures 8(a) and 8(c) show a comparison of $E_{\text{noise}}^{\text{dir}}$ and $\bar{E}_{\text{noise}}^{\text{dir}}$, calculated using Eq. (52). The analytical results agree well with the simulations for small $\sigma_{\text{in}}/\Delta f$ but, as expected, deviate for larger $\sigma_{\text{in}}/\Delta f$. Figures 8(b) and 8(d) show that the analytical estimates can be significantly improved by employing Eq. (54).

The results for $E_{\text{noise}}^{\text{abs}}$ are shown in Fig. 9, again highlighting that there is good agreement between the analytical results and those obtained by reconstructing the vector potential from simulated micrographs.

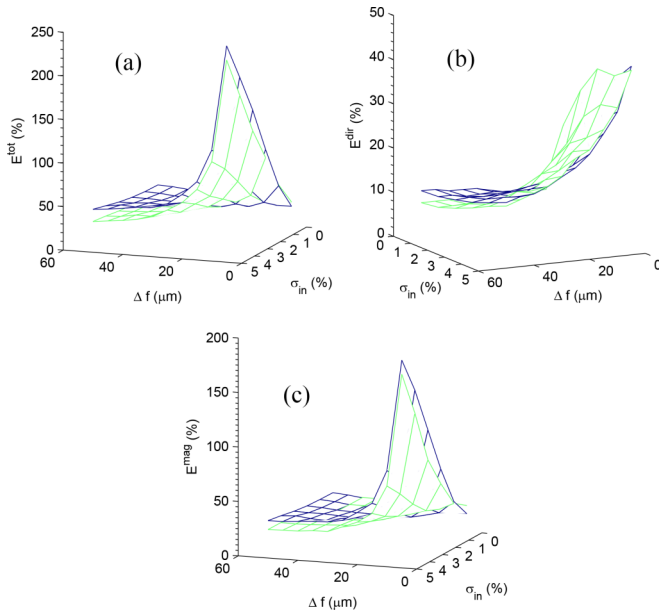


FIG. 10. (Color online) Surface plots showing reconstruction errors (a) E^{tot} , (b) E^{dir} , and (c) E^{mag} . Each subfigure shows both the results obtained using Eq. (5) for the phase retrieval, in blue (black), and Eq. (6), in green (gray).

E^{tot} , E^{dir} , and E^{mag} are shown as surface plots in Fig. 10. These can be compared with the extracted noise induced errors shown in Figs. 7–9 to see how significant the noise-induced component of the total error is in relation to the combined contribution of all other sources of error.

V. CONCLUSION

Shot noise is an unavoidable source of error in any imaging process. In VFET, shot noise in the micrographs results in errors in both the magnitude and direction of the reconstructed vector potential. An understanding of the relationship between image noise and the accuracy of VFET reconstructions provides various benefits. For a particular application, there may be a maximum tolerable error in a tomographic reconstruction. Understanding the propagation of noise through the reconstruction algorithm, combined with an understanding of other sources of error, will provide a maximum allowable noise level in the micrographs. This in turn will enable determination of a minimum acquisition time per image, allowing for minimal sample degradation and microscope time.

The results presented in Sec. IV show that the propagation of noise in VFET can be accurately quantified for a given reconstruction algorithm, including any regularization scheme, and a known noise level and spatial frequency spectrum. For our simulations, we have used a shot-noise model in which the variance of the noise at each pixel in each image used in the reconstruction is dependent on the intensity of the electron beam. For this reason, the spatial dependence of the noise level is also a function of tilt angle, so the power spectrum of the noise is, in practice, a complicated function of spatial frequencies and tilt angle. However, we have shown shot noise to be adequately modeled as white noise for the purposes of analyzing propagation of errors in the reconstruction. There are other factors that can be taken into account in determining a value for the noise filters used for analytical calculations of VFET reconstruction errors, in cases where setting it to unity is not sufficient. One possible example is the blurring of shot noise in the detector, which is commonly modeled using a modulation transfer function [48] or noise transfer function [49], which could be incorporated into these filter functions. A filtered noise model may be useful for determining the contribution of other stochastic error sources, such as thermal detector noise, and the power spectral density of these noise sources would typically be independent of tilt series and tilt angle, allowing a simple two-dimensional filter to be used in the noise analysis.

With modification, the noise analysis presented here can be used for many other calculations of noise-induced errors in reconstructions where linear, Fourier-transform methods have been employed. This includes, but is not limited to, those arising from other VFET algorithms, as well as scalar tomography and phase retrieval algorithms.

We have derived expressions for the total, directional, and magnitude rms noise-induced errors in vector fields reconstructed from transmission electron micrographs using an FBP algorithm. The results of simulations presented here show that noise-induced errors can be quickly computed to accurately estimate their contribution to the total rms errors in a VFET reconstruction.

ACKNOWLEDGMENTS

The authors acknowledge use of facilities within the Monash Centre for Electron Microscopy, and financial support

from the Australian Research Council. We would also like to thank R. P. Yu for providing code used for simulations in this work. Z. D. C. Kemp is supported by a Monash University Faculty of Science Dean's Postgraduate Research Scholarship.

-
- [1] S. J. Lade, D. Paganin, and M. J. Morgan, *Opt. Commun.* **253**, 382 (2005).
 - [2] C. Phatak, A. K. Petford-Long, and M. De Graef, *Phys. Rev. Lett.* **104**, 253901 (2010).
 - [3] R. P. Yu, M. J. Morgan, and D. M. Paganin, *Phys. Rev. A* **83**, 023813 (2011).
 - [4] S. A. Wolf, D. D. Awschalom, R. A. Buhrman, J. M. Daughton, S. von Molnr, M. L. Roukes, A. Y. Chtchelkanova, and D. M. Treger, *Science* **294**, 1488 (2001).
 - [5] A. Akbarzadeh, M. Samiei, and S. Davaran, *Nanoscale Res. Lett.* **7**, 1 (2012).
 - [6] S. N. Piramanayagam, M. Ranjbar, R. Sbiaa, A. Tavakkoli, and T. C. Chong, *Phys. Status Solidi RRL* **6**, 141 (2012).
 - [7] S. Bamrungsap, J. A. Phillips, X. Xiong, Y. Kim, H. Wang, H. Liu, A. Hebard, and W. Tan, *Small* **7**, 601 (2011).
 - [8] M. R. Scheinfein, P. J. Ryan, J. Unguris, D. T. Pierce, and R. J. Celotta, *Appl. Phys. Lett.* **57**, 1817 (1990).
 - [9] A. Schwarz and R. Wiesendanger, *Nano Today* **3**, 28 (2008).
 - [10] R. Wiesendanger, *Rev. Mod. Phys.* **81**, 1495 (2009).
 - [11] M. De Graef, in *ESOMAT 2009: 8th European Symposium on Martensitic Transformations*, edited by P. Šittner, V. Paidar, L. Heller, and H. Seiner (EDP Sciences, Les Ulis, France, 2009).
 - [12] S. J. Lade, D. Paganin, and M. J. Morgan, *Opt. Commun.* **253**, 392 (2005).
 - [13] R. Zehbe, A. Haibel, H. Riesemeier, U. Gross, C. J. Kirkpatrick, H. Schubert, and C. Brochhausen, *J. R. Soc., Interface* **7**, 49 (2010).
 - [14] J. Frank, *Electron Tomography: Three-dimensional Imaging with the Transmission Electron Microscope* (Plenum, New York, 1992).
 - [15] C. Kübel, A. Voigt, R. Schoenmakers, M. Otten, D. Su, T.-C. Lee, A. Carlsson, and J. Bradley, *Microsc. Microanal.* **11**, 378 (2005).
 - [16] M. Richards, J. Budaj, M. Agafonov, and O. Sharova, in *Binaries—Key to Comprehension of the Universe*, edited by A. Prsa and M. Zejda (Astronomical Society of the Pacific, Orem, UT, 2010), Vol. 435, pp. 77–80.
 - [17] J. M. Lees, *J. Volcanol. Geotherm. Res.* **167**, 37 (2007).
 - [18] Y. S. Kashyap, A. Agrawal, P. S. Sarkar, M. Shukla, and A. Sinha, *AIP Conf. Proc.* **1512**, 452 (2013).
 - [19] S. J. Norton, *IEEE Trans. Image Process.* **1**, 406 (1992).
 - [20] T. Jansson, M. Almqvist, K. Strahlen, R. Eriksson, G. Sparr, H. Persson, and K. Lindstrom, *Ultrasound Med. Biol.* **23**, 47 (1997).
 - [21] H. Sielschott, *Flow Meas. Instrum.* **8**, 191 (1998).
 - [22] G. D'Antona, in *IMTC 2002, Proceedings of the 19th IEEE Instrumentation and Measurement Technology Conference, Anchorage, Alaska, 2002* (IEEE, Piscataway, NJ, 2002), Vol. 1, pp. 581–585.
 - [23] E. Snoeck, C. Gatel, L. M. Lacroix, T. Blon, S. Lachaize, J. Carrey, M. Respaud, and B. Chaudret, *Nano Lett.* **8**, 4293 (2008).
 - [24] D. Paganin and K. A. Nugent, *Phys. Rev. Lett.* **80**, 2586 (1998).
 - [25] C. Phatak, Ph.D. thesis, Carnegie Mellon University, 2009.
 - [26] Y. Aharonov and D. Bohm, *Phys. Rev.* **123**, 1511 (1961).
 - [27] M. R. Teague, *J. Opt. Soc. Am.* **73**, 1434 (1983).
 - [28] R. W. Gerchberg and W. O. Saxton, *Optik* **35**, 237 (1972).
 - [29] T. E. Gureyev and K. A. Nugent, *Opt. Commun.* **133**, 339 (1997).
 - [30] D. Paganin, A. Barty, P. J. McMahon, and K. A. Nugent, *J. Microsc. (Oxford, UK)* **214**, 51 (2004).
 - [31] A. Kohn, A. K. Petford-Long, and T. C. Anthony, *Phys. Rev. B* **72**, 014444 (2005).
 - [32] V. V. Volkov and Y. Zhu, *Ultramicroscopy* **98**, 271 (2004).
 - [33] A. Tonomura, T. Matsuda, J. Endo, T. Arii, and K. Mihama, *Phys. Rev. B* **34**, 3397 (1986).
 - [34] E. Humphrey, C. Phatak, A. Petford-Long, and M. De Graef, *Ultramicroscopy* **139**, 5 (2014).
 - [35] C. Phatak, M. Beleggia, and M. De Graef, *Ultramicroscopy* **108**, 503 (2008).
 - [36] W. H. Press, S. A. Teukolsky, W. T. Vetterling, and B. P. Flannery, *Numerical Recipes in C: The Art of Scientific Computing*, 2nd ed. (Cambridge University Press, Cambridge, England, 1992), Chap. 12.
 - [37] T. E. Gureyev, A. Pogany, D. M. Paganin, and S. W. Wilkins, *Opt. Commun.* **231**, 53 (2004).
 - [38] V. A. Vinokurov, in *Ill-posed Problems in the Natural Sciences*, edited by A. N. Tikhonov and A. V. Goncharsky (Mir Publishers, Moscow, 1987).
 - [39] L. Reimer and H. Kohl, in *Transmission Electron Microscopy: Physics of Image Formation*, 5th ed. (Springer, New York, 2008), p. 96.
 - [40] E. J. McDowell, X. Cui, Z. Yaqoob, and C. Yang, *Opt. Express* **15**, 3833 (2007).
 - [41] K. M. Spiers, J. D. Cashion, and K. A. Gross, *Key Eng. Mater.* **254**, 213 (2004).
 - [42] T. C. Petersen and S. P. Ringer, *Comput. Phys. Commun.* **181**, 676 (2010).
 - [43] See Supplemental Material at <http://link.aps.org/supplemental/10.1103/PhysRevA.90.023859> for an animation of the simulated sample, overlaid with the experimental tomograms.
 - [44] R. J. Harrison, R. E. Dunin-Borkowski, and A. Putnis, *Proc. Natl. Acad. Sci. USA* **99**, 16556 (2002).
 - [45] N. Mizutani, T. Iwasaki, S. Watano, T. Yanagida, H. Tanaka, and T. Kawai, *Bull. Mater. Sci.* **31**, 713 (2008).
 - [46] S. Si, A. Kotal, T. K. Mandal, S. Giri, H. Nakamura, and T. Kohara, *Chem. Mater.* **16**, 3489 (2004).
 - [47] R. P. Yu and D. M. Paganin, *New J. Phys.* **12**, 073040 (2010).
 - [48] H. Rullgård, L.-G. Öfverstedt, S. Masich, B. Daneholt, and O. Öktem, *J. Microsc. (Oxford, UK)* **243**, 234 (2011).
 - [49] R. R. Meyer and A. I. Kirkland, *Microsc. Res. Tech.* **49**, 269 (2000).